Analytical Modeling and Inverse Design of Centimeter-Scale Hard-Magnetic Soft Robots

Jinqiang Wang, Dong Wang, Le Dong, Mengjie Zhang, and Guoying Gu, *Senior Member, IEEE*

***Abstract*— Hard-magnetic soft robots can form diverse soft-body deformation modes and safely interact with their surrounding environment, offering great promise in performing complex functions. Although there have been significant theoretical developments of small-scale soft robots, the design of centimeter-scale soft robots with larger workspace and output forces remains elusive. In this paper, we develop an analytical model to automatically design centimeter-scale hard-magnetic soft robots that exhibit desired configurations, enabled by programming the magnetization profile. The model considers the varying magnetization profile, gravity effect and large deformation, and directly relates the material, geometric and loading parameters to the final configurations. We develop an inverse design method for configuration matching based on the theoretical model. We demonstrate soft robots designed by the theoretical model with the capability to pass through narrow channels and crawl over obstacles. We further demonstrate optimized soft grippers showing conformal grasping of complex objects. The proposed methodology paves the way to design centimeter-scale soft robots and broaden their applications.**

***Note to Practitioners*—The motivation of this work is to analyze, predict, and control the centimeter-scale hard-magnetic soft robot under external magnetic fields. While smaller magnetic-driven soft robots have been extensively studied, the centimeter-scale soft robots offer larger workspace and output forces, making them more versatile for certain applications. This paper develops an analytical model for centimeter-scale hard-magnetic soft robots that takes into account the varying magnetization profile, gravity effect and large deformation. It allows magnetically driven soft robots to pass through narrow channels and crawl over obstacles. In addition, an optimization method is proposed by virtue of the analytical model, enabling the inverse design of soft robots with prescribed grasping postures. The analytical model and optimization method can be implemented for the dexterous locomotion and manipulation of magnetic soft robots with large workspace and output forces in medical and industrial settings.**

***Index Terms*— Soft robotics, hard-magnetic, soft material, analytical model, inverse design.**

Manuscript received 16 July 2023; accepted 4 September 2023. This article was recommended for publication by Associate Editor T. Xu and Editor L. Zhang upon evaluation of the reviewers' comments. This work was supported in part by the National Key Research and Development Program of China under Grant 2022YFB4700900, in part by the National Natural Science Foundation of China under Grant 52025057 and Grant 52275025, and in part by the State Key Laboratory of Mechanical System and Vibration under Grant MSVZD202212. *(Corresponding author: Dong Wang.)*

The authors are with the State Key Laboratory of Mechanical System and Vibration, the School of Mechanical Engineering, and the Meta Robotics Institute, Shanghai Jiao Tong University, Shanghai 200240, China (e-mail: wangjq_sjtu@sjtu.edu.cn; wang_dong@sjtu.edu.cn; dong_le@sjtu.edu.cn; TakiyaGenji27@sjtu.edu.cn; guguoying@sjtu.edu.cn).

This article has supplementary material provided by the authors and color versions of one or more figures available at https://doi.org/10.1109/TASE.2023.3313395.

Digital Object Identifier 10.1109/TASE.2023.3313395

I. Introduction

THE hard-magnetic soft material (HMSM) can realize complex shape transformations due to the high coercivity in contrast to the soft-magnetic materials. HMSM is generally obtained by embedding hard-magnetic particles (e.g., neodymium-iron-boron alloy, NdFeB) into a soft polymeric matrix (e.g., silicone rubber, gels) [1], [2], [3]. Untethered, reversible, rapid and programmable actuation can be induced by manipulating the internal magnetization profiles and external magnetic field [4], [5], [6], [7], [8], [9], [10], [11], [12], [13], [14], [15], [16], which are essential for performing soft robotic functions such as grasping [17], [18], walking [8], [19], swimming [20], [21], jumping [7], [8], transporting [22], [23], climbing [24], [25], and navigation [9], [26].

Several pioneering works have been proposed to program the configurations of the HMSM [2], [3], [27], [28], [29], [30]. For example, a nonlinear beam model is developed based on force and moment equilibriums, enabling the generation of continuum magnetization profiles for desired time-varying shapes [2]. A theoretical model for hard-magnetic soft beams is developed based on nonlinear elasticity and implemented the model in commercial finite-element software [3], [28]. Hard-magnetic rods under geometrically nonlinear deformation in three dimensions are modeled using a Kirchhoff-like theory [29]. Analytical models based on the rod theory are also used to investigate the 2D and 3D deformations [31], [32], [33], [34]. A finite deformation, constitutive model is proposed taking into account the microstructural characteristics of HMSM [35], [36]. Additionally, the design freedoms of HMSM are exploited using optimized-based or data-driven approaches [19], [37], [38], [39]. The above works provide systematic design methods for small-scale hard-magnetic soft robots. However, bottlenecks exist in manufacturing and assembly when the soft robot is scaled down to millimeter size. Moreover, workspace and output force are limited for small-scale soft robots, which limits their ability to fulfill complex tasks in unstructured environments. As a result, centimeter-scale soft robots with larger workspace and output forces are desired, which haven't attracted enough interest yet.

The gravity effect is generally ignored for small-scale hard-magnetic soft robots (length less than 5 mm typically) [2], [3], [7], [8]. As the size of a HMSM soft robot increases to the centimeter scale, gravity significantly affects the deformations as it is intrinsically soft, which alters performances such as rolling, bending and crawling [32], [40], [41]. On the other hand, continuously varying magnetization profiles can be

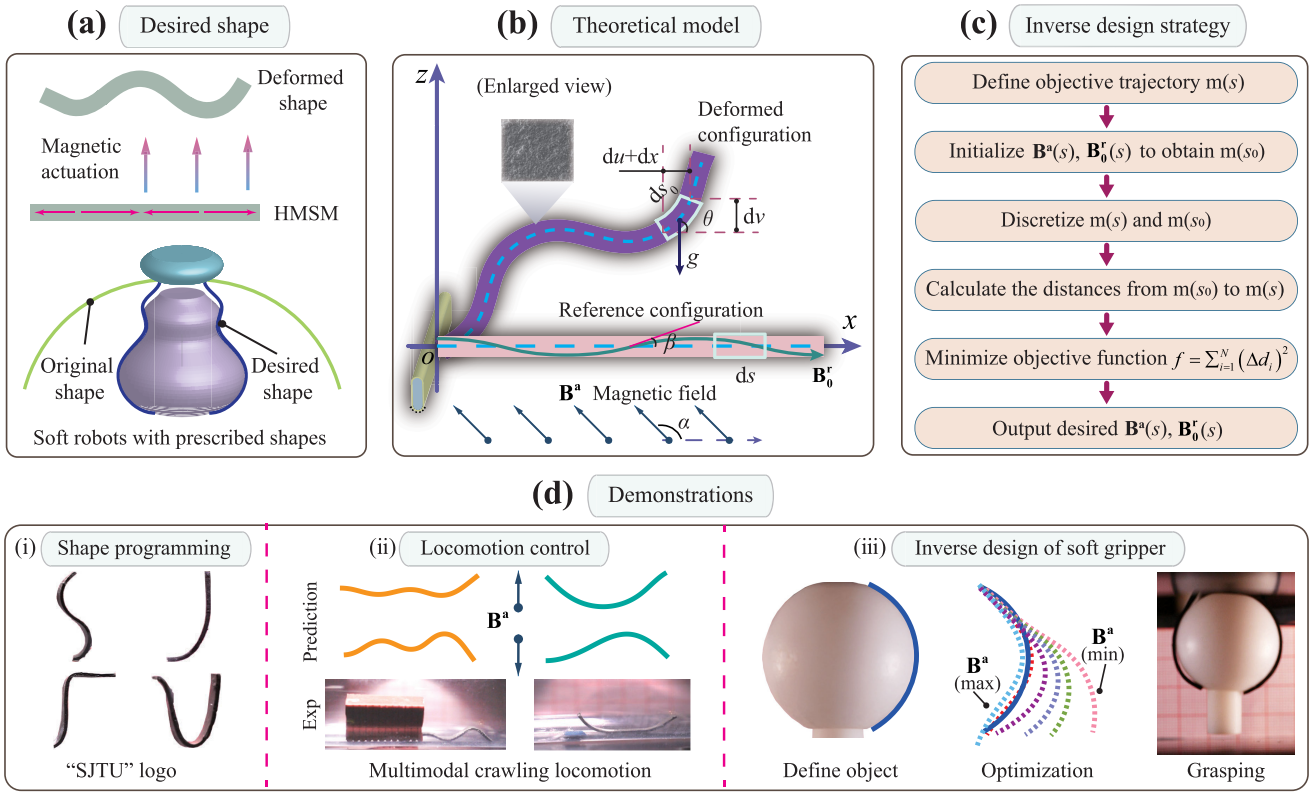

Fig. 1. Design of untethered soft robots.(a) Under the magnetic actuation, the HMSM aligns its orientation with the applied field inducing shape deformation. A desired shape is given. (b) A theoretical model is developed to predict the deformed configurations of a HMSM beam subjected to uniform magnetic fields. (c) The inverse design procedures. (d) Experimental demonstrations of the modeling and inverse design methods, including (i) "SJTU" shapes, (ii) multimodal HMSM soft robots and (iii) a soft gripper with prescribed shape.

easily imposed on the centimeter-scale soft robots, increasing the diversity of soft-body deformation modes. For instance, recent advances in manufacturing methods have enabled varying magnetization profiles by pre-designed jigs [2], [8], [10] or direct ink writing 3D printing [1], [18], [19], [42]. Compared to the uniform or alternating magnetization profiles, continuously varying magnetization profiles can form complex shapes, which fulfill the multimodal grasping and locomotion requirements of soft robots [2], [8], [10], [29]. A recent study considers the varying magnetization profiles but neglects the gravity effect [2]. Therefore, theoretical models and design methods that take into account the varying magnetization profiles and gravity effect are needed to predict and design centimeter-scale soft robots' complex configurations accurately.

In this work, we develop an analytical model and inverse optimization method to design the centimeter-scale hard-magnetic soft robots. Under the magnetic actuation, the HMSM aligns its orientation with the applied field inducing shape deformation (Fig. 1(a)). To obtain a desired shape, we develop a theoretical model that takes into account the varying magnetization profile, gravity effect and large deformation based on the minimum potential energy (Fig. 1(b)). The potential energy of the HMSM contains three parts: Helmholtz's energy considering varying magnetization profiles, elastic energy incorporating the large deformation and gravitational energy representing the gravity effect. The theoretical model directly relates the input parameters (magnetization profile and applied magnetic field) to the final deformation, which can be used to program the deformed configurations. Additionally, an optimization method is proposed by virtue of the analytical model, enabling the inverse design of soft robots with specific deformations (Fig. 1(c)). Using the developed analytical model and inverse optimization method, in Fig. 1(d), we demonstrate (i) HMSM beams deformed into a "SJTU" logo, (ii) multimodal crawling soft robots and (iii) soft grippers matching the complex surface.

The main contribution of this work can be summarized as follows. (i) We develop an analytical model for centimeter-scale HMSM that takes into account the varying magnetization profiles, gravity effect and large deformation. (ii) An inverse design method is developed based on the analytical model to optimize the HMSM deformed configurations. (iii) This work develops a complete workflow from the analytical modeling, experimental validation, and inverse optimization to soft robot demonstrations. The paper is organized as follows. We first present the manufacturing process of the HMSM and then develop a theoretical model and an optimization method, followed by theory validations. HMSM beams with programmed shapes and multimodal crawling soft robots are then demonstrated. The inversely designed soft grippers are shown by grasping and lifting experiments.

II. Theory and Optimization Method

The HMSM with varying magnetization profiles is schematically shown in Fig. S1. The HMSM is realized by mixing NdFeB microparticles (an average size of $\sim 5\mu$m) homogeneously into uncured silicone elastomer (Ecoflex 00-10). After curing, the magnetic dipoles within the HMSM are random and cannot induce a programmable magnetic response. To generate a controllable magnetization profile, the HMSM is magnetized to saturation under an impulse field (about 2 Tesla) within a jig as shown in Fig. S2. The high coercivity (Fig. S3) ensures the magnetic dipoles are aligned after the magnetization field is removed. Each dipole produces a local response when an actuating field is applied, which deforms the HMSM (Fig. 1b). The deformation of HMSM can then be programmed by adjusting the magnetization profile, represented by the residual magnetic flux density vector $\mathbf{B_0^r}$ of the HMSM.

Owing to the large aspect ratio of HMSM, it is reasonable to define $\mathbf{B_0^r}$ as a function of the length s. s is the coordinate along the HMSM beam's arc-length. If a continuum magnetization profile is desired, the shape coordinates $[x_{\text{jig}}, z_{\text{jig}}]$ of the jig can be designed as [2]:

$$\begin{aligned} x_{\text{jig}} &= \int_0^s \cos(\psi(s))\mathrm{d}s, \\ z_{\text{jig}} &= \int_0^s \sin(-\psi(s))\mathrm{d}s, \end{aligned} \tag{1}$$

where $\psi(s)$ is the slope angle of $\mathbf{B_0^r}$. According to previous work, both B^{r} (the magnitude of $\mathbf{B_0^r}$) and the elastic modulus of HMSM beam E depend on the volume fraction $\varphi(s)$ [3], [9], [33], [43]:

$$B^{\text{r}}(s) = B_{\text{p}}^{\text{r}}\varphi(s), \tag{2}$$

$$E(s) = E_0 \exp\left(\frac{2.5\varphi(s)}{1-1.35\varphi(s)}\right), \tag{3}$$

where B_{p}^{r} denotes the magnitude of residual magnetic flux density of NdFeB particles, and E_0 is the elastic modulus of the elastomer. No apparent aggregation or phase separation is observed in the scanning electron microscope images of HMSM beams with different particle volume fractions (Fig. S3), thereby permitting the usage of continuum assumption when describing their macroscopic behaviors.

A theoretical framework based on the minimum potential energy method is developed. A cantilevered HMSM beam subjected to a uniform external magnetic field is considered. The undeformed and deformed shapes are shown in Fig. 1(b). The beam has a length l, a cross-section area A, a density ρ, an elastic modulus E and rotational inertia I. The Cartesian coordinate's origin is set at the left end of the undeformed beam with the x-axis along the length direction and the z-axis along the height direction. Upon deformation, the infinitesimal segment at the centroid axis varies from $\mathrm{d}s$ to $\mathrm{d}s_0$. The residual magnetic flux density vector continuously varies along the beam, whose direction forms an angle $\beta(s)$ to the x-axis. Therefore, $\mathbf{B_0^r}$ can be written as:

$$\mathbf{B}_0^{\text{r}} = B^{\text{r}}\cos\beta\mathbf{i} + B^{\text{r}}\sin\beta\mathbf{k}, \tag{4}$$

where $\mathbf{i}$ and $\mathbf{k}$ denote the unit vectors in the x-direction and z-direction, respectively. The external magnetic field $\mathbf{B^a}$ is expressed as:

$$\mathbf{B^a} = B^{\text{a}}\cos\alpha\mathbf{i} + B^{\text{a}}\sin\alpha\mathbf{k}, \tag{5}$$

where α is the angle between $\mathbf{B^a}$ and the x-axis, B^{a} is the magnitude of $\mathbf{B^a}$.

The Euler-Bernoulli beam theory is used. The planar deformation can be represented by the horizontal displacement u and vertical displacement v of the centerlines:

$$u = \int_0^s [(1+\varepsilon)\cos\theta - 1]\mathrm{d}s, \tag{6}$$

$$v = \int_0^s (1+\varepsilon)\sin\theta\mathrm{d}s, \tag{7}$$

where θ and ε are the rotational angles between the centerline and x-direction, and the axial strain of the beam centerline, respectively. ε can be calculated as ε=(ds-ds_0)/ds. The magnetic potential energy density of the HMSM beam is

$$W^{\text{m}}\left(\mathbf{F}, \mathbf{B_0^r}, \mathbf{B^a}\right) = -\frac{1}{\mu_0}\mathbf{F}\mathbf{B_0^r}\cdot\mathbf{B^a}, \tag{8}$$

where μ_0 is the vacuum permeability and $\mathbf{F}$ is the deformation gradient. Under the external field, a point $[x, 0]$ deforms to $[u{+}x, v]$. $\mathbf{F}$ is then calculated as

$$\mathbf{F} = \frac{\mathrm{d}[x+u, v]^{\text{T}}}{\mathrm{d}[x, 0]^{\text{T}}} = \begin{bmatrix}(1+\varepsilon)\cos\theta & 0\\ (1+\varepsilon)\sin\theta & 0\end{bmatrix}, \tag{9}$$

where T denotes the transpose of the vectors. By substituting (4), (5) and (9) into (8), the stored Helmholtz's energy of a HMSM beam is calculated by a volume integration [3]:

$$\begin{aligned} U_{\text{m}} &= \int_A\int_0^l W^{\text{m}}\mathrm{d}s\mathrm{d}A \\ &= -\frac{A}{\mu_0}\int_0^l (1+\varepsilon)B^{\text{r}}B^{\text{a}}\cos(\theta-\alpha)\cos\beta\mathrm{d}s. \end{aligned} \tag{10}$$

The elastic energy U_{s} of the HMSM beam consists of the bending and stretching energies. During the shape change, the bending deformation is dominative while the axial strain is small, which allows us to postulate the small strain assumption in calculating the strain energy [31], [33]. Therefore,

$$U_{\text{s}} = \int_0^l \frac{EA}{2}\varepsilon^2\mathrm{d}s + \int_0^l \frac{EI}{2}\left(\frac{\mathrm{d}\theta}{\mathrm{d}s}\right)^2\mathrm{d}s. \tag{11}$$

As the beam is slender and soft, gravity plays a vital role in its deformation. The gravitational potential energy of the HMSM beam is considered as

$$\begin{aligned} U_{\text{g}} &= -\rho Ag\int_0^l v\mathrm{d}s \\ &= -\rho Ag\int_0^l\int_0^s (1+\varepsilon)\sin\theta\mathrm{d}s\mathrm{d}s, \end{aligned} \tag{12}$$

where g is the gravitational constant. The usage of the principle of minimum potential energy

$$\delta\left(U_{\text{m}} + U_{\text{s}} + U_{\text{g}}\right) = 0, \tag{13}$$

leads to the following governing equations:

$$\delta\varepsilon : EA\varepsilon - \frac{A}{\mu_0} B^{\mathrm{r}} B^{\mathrm{a}} \cos(\theta-\alpha)\cos\beta - \rho A g (l-s)\sin\theta = 0, \tag{14}$$

$$\delta\theta : \frac{\mathrm{d}}{\mathrm{d}s}\left(EI\frac{\mathrm{d}\theta}{\mathrm{d}s}\right) - (1+\varepsilon)\frac{A}{\mu_0} B^{\mathrm{r}} B^{\mathrm{a}} \sin(\theta-\alpha)\cos\beta + \rho A g (l-s)(1+\varepsilon)\cos\theta = 0. \tag{15}$$

The corresponding boundary conditions are

$$\theta = 0 \text{ or } \theta' = 0 \text{ at } s = 0 \text{ and } l, \tag{16}$$

for the clamped boundary and free boundary, respectively. It should be noted that the Semler equation is used to obtain the governing equations [44]. By substituting (2), (3) into (14), (15) with the boundary conditions, the two unknowns θ and ε can be solved. Finally, the deformed shape of the HMSM beam can be calculated based on (6), (7) by

$$X = s + u, \quad Z = v. \tag{17}$$

Here, the coordinate (X, Z) denotes an arbitrary point on the beam centerline in the deformed configuration. The rotation angle and axial strain can be obtained by solving the governing Equations (14) and (15) with boundary conditions. The displacements of the beam centerline can be determined by Equations (6) and (7). The deformed configuration of the HMSM beam can be calculated using Equation (17). The implementation of predicting HMSM deformation with the developed model is summarized as Algorithm 1 in the Appendix.

Based on the above analytical theory, an inverse design strategy is proposed. The objective shape is extracted from the contour of the given object, and then discretized into a set of points. We assume that the HMSM beam possesses the same length as the object contour. m(s) (the direction of $\mathbf{B_0^r}$) and B^{a} (the magnitude of $\mathbf{B^a}$) are selected as the optimization parameters. The optimal m(s) and $\mathbf{B^a}$ are obtained by minimizing the objective function f with constraints:

$$\min_x \ f \qquad s.t.: \ B_{\min} \le B^a \le B_{\max} \tag{18}$$

where $f = \sum_{i=1}^{N} (\Delta d_{\mathrm{i}})^2$ represents the summation of the square distances between the objective and calculated centerlines. N equally distributed points are chosen on the objective curve. Δd_{i} is the minimum distance of point i to the theoretically calculated curve. The function "fmincon" in Matlab is used for the optimization [45]. To simplify the optimization process, B^{a} is applied perpendicularly to the initial length of HMSM beams. m(s) consists of the elementary functions with variable parameters. The ranges of the variable parameters are also bounded in the optimization. The detailed inverse design method is demonstrated as Algorithm 2 in the Appendix. Specifically, soft grippers following objective trajectories are optimized in our experiments to grasp the objects with an enhanced lifting capacity.

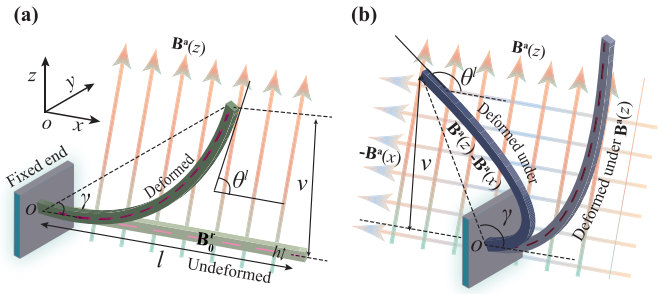

Fig. 2. Schematic of a cantilevered HMSM beam bending with a uniform magnetization profile. An increasing $\mathbf{B^a}(z)$ is applied first in (a), and an increasing -$\mathbf{B^a}(z)$ is applied next in (b).

III. Model Validation

Experiments are conducted to validate the analytical model. Cantilevered HMSM beams with a uniform magnetization profile $\mathbf{B_0^r}$ (aligned with x-direction) and a constant particle volume fraction $\varphi(x)$ are tested. Two external fields are applied: (a) an increasing uniform $\mathbf{B^a}(z)$; (b) an increasing uniform -$\mathbf{B^a}(x)$ with a constant $\mathbf{B^a}(z)$, as shown in Fig. 2 and Movie 1. Here $\mathbf{B^a}(x)$ and $\mathbf{B^a}(z)$ represent the applied magnetic field intensity in the x and z directions. Due to the non-constant curvature of the deformed shapes, three parameters are used to compare the experimental and theoretical results: the vertical displacement at the tip v, the tangent angle at the tip θ^l and the overall rotation angle γ.

To characterize the mechanical and magnetic properties of the HMSM, the magnetization magnitude M=B^{r}/μ_0 and the Young's modulus E are measured for HMSM with different particle volume fractions φ in Fig. S2B and Fig. S4. The measurement methods are detailed in Supplementary Materials S1. By fitting (2) and (3), the parameters are obtained as E_0=0.062 MPa and $B_{\mathrm{p}}^{\mathrm{r}}$=575 kA/m, which falls in reasonable ranges [1], [9], [46].

The theoretical and experimental deformed shapes under varying magnetic fields are compared. The material and geometric parameters are length l=25 mm, width w=5 mm, height h=1.13 mm, particle volume ratio φ=20% and density ρ=1.94 g/cm^3. The comparison between the experimental and analytical shapes with different aspect ratios l/h = 17.7 and 26.5 are shown with the specific magnetic strengths in Fig. S5 and Movie 2. The theoretical shapes show well agreement with experiments for all three samples. The effect of gravity can be clearly observed in the experiments, especially under low applied fields and for beams with large aspect ratios. For comparison, the theoretical deformed shapes without gravity are given in Fig. S5. Large discrepancies exist, especially with low applied fields, showing that gravity cannot be neglected.

For quantitative comparison, theoretical and experimental v/l, θ^l and γ are plotted in Fig. 3 against the normalized applied magnetic field P for three HMSM beams with l/h = 17.7, 22.1 and 26.5. P is normalized as $B^a B_{\mathrm{p}}^{\mathrm{r}} A l^2 / E_0 \mu_0 I$. v/l is the normalized deflection. φ is fixed as 20%. Details of the normalization process are given in Supplementary Materials S2.

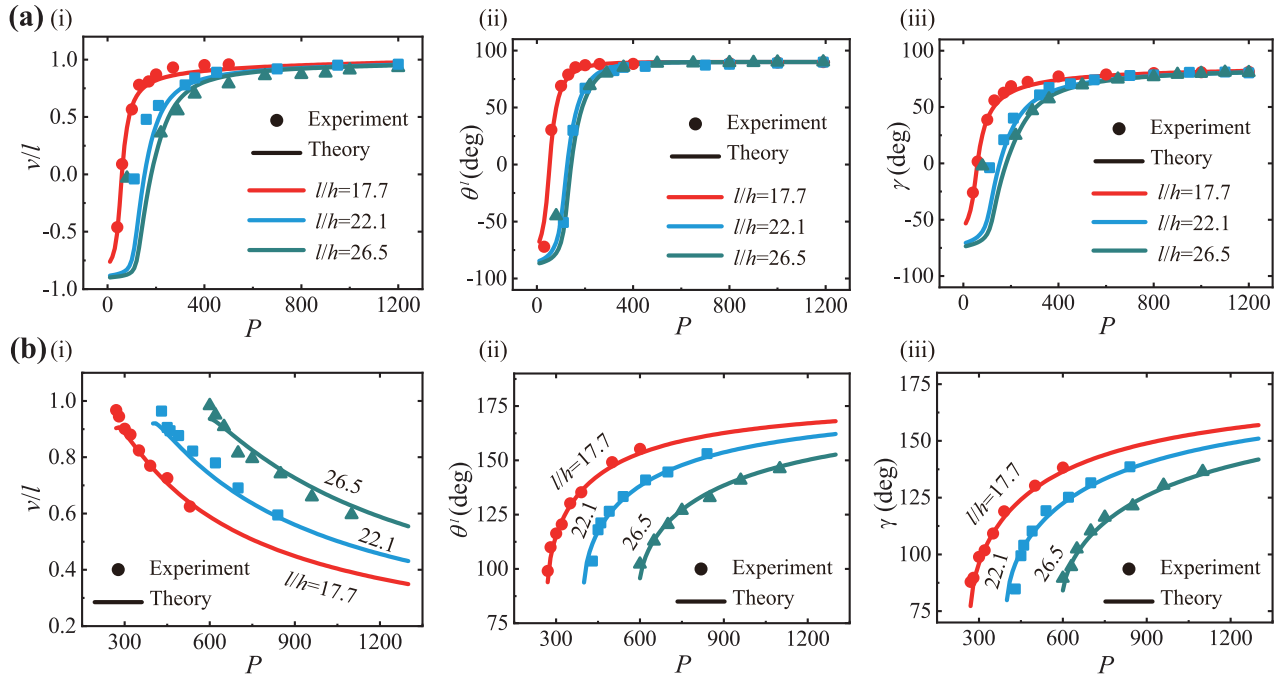

Fig. 3. Experimental validation of theoretical model. The theoretical (solid lines) and experimental (symbol dots) (i) normalized deflection v/l, (ii) tangent angle θ^l and (iii) overall rotation angle γ on the normalized magnetic field P, with (a) an increasing $\mathbf{B}^{\mathbf{a}}(z)$ (0 to 13 mT) and (b) an increasing $\mathbf{B}^{\mathbf{a}}(x)$ (0 to -22 mT) superposed on a constant $\mathbf{B}^{\mathbf{a}}(z)$. Dashed lines mark the neutral axes. Scale bars are 5 mm.

In Fig. 3(a), an increasing $\mathbf{B}^{\mathbf{a}}(z)$ (from 0 to 13 mT) is applied. It is found that all three parameters (v/l, θ^l and γ) increase monotonically with P. As P increases, v/l is closed to 1 and θ^l and γ approach 90°. All three parameters increase fast initially and then become nearly flattened. The parameters decrease with the aspect ratio, indicating that the HMSM shows a smaller deflection due to the gravity effect. The influence of the aspect ratio reduces as the magnetic field strength increases. We subsequently shift the bending of HMSM beams from vertical to horizontal by increasing $\mathbf{B}^{\mathbf{a}}(x)$ from 0 to -22 mT while fixing a large $\mathbf{B}^{\mathbf{a}}(z)$. As shown in Fig. 3(b), when the additional $\mathbf{B}^{\mathbf{a}}(x)$ is applied, v/l decreases monotonically, while both θ^l and γ keep increasing to 180°. It can be observed that the theoretical results (solid line) agree well with the experimental results (symbol dot). The experimental and theoretical predicted deformed shapes with varying particle volume fraction φ are studied in Fig. S6 and Movie 3.

IV. Experimental Demonstration

A. Programming Deformed Shapes of HMSM Beams

The validated theoretical model is then used to program the deformed configurations of the HMSM beams by varying the magnetization profile $\mathbf{B}_{\mathbf{0}}^{\mathbf{r}}$. HMSM beams with four or six magnetic unit cells assembled are designed, as shown in Fig. 4(a). The magnetic unit cells are connected using silicone joints with alternating magnetization directions. The deformed configurations of the HMSM beams under a switching magnetic field ($\mathbf{B}^{\mathbf{a}}(z)$=±11.42 mT or ±14.42 mT) are shown. Mountains or valleys are formed due to the alternating magnetization directions in adjacent units (Movie 4). The corresponding analytical results are obtained with free boundary conditions at both ends for comparison. The analytical model predicts well the experimental shapes.

Next, the HMSM beams with continuously varying $\mathbf{B}_{\mathbf{0}}^{\mathbf{r}}$ are designed and their shapes are predicted. The beams are magnetically saturated using jigs with predetermined shapes. In Fig. 4(b)-(d), three different jigs are used for magnetization. Their trajectory coordinates [x_{jig}, z_{jig}] satisfy a quadratic function $z = 0.1(x-20)^2$ (Fig. 4(b)), a sinusoidal function $z = 15\sin(0.05\pi x)$ (Fig. 4(c)), and a piecewise function $z = \{-0.2(x-10)^2+20, x < 20; -10\sin(0.2\pi(x-20)), x \geq 20\}$ (Fig. 4(d)). The produced magnetization profiles are obtained using (1). The deformed experimental configurations under increasing $\mathbf{B}^{\mathbf{a}}$ are shown with analytical results overlapped for comparison. It can be seen that all of the theoretical results agree well with the experimental results. Some discrepancies exist, possibly due to the nonuniform distribution of the applied magnetic fields, inhomogeneous particle distributions and manufacturing errors. Although the magnetic actuation is a function of $\mathbf{B}_{\mathbf{0}}^{\mathbf{r}}$ and $\mathbf{B}^{\mathbf{a}}$, it is more feasible to regulate the orientation of $\mathbf{B}_{\mathbf{0}}^{\mathbf{r}}$ while setting $\mathbf{B}^{\mathbf{a}}$ to be uniform in the workspace, considering the difficulty of manipulation in practice. In Fig. 4(e), the magnetization profiles are varied to form intricated configurations. By properly designing the magnetization profiles, four HMSM beams form the "SJTU" logo shape under vertical magnetic fields (Movie 5). The above results show that the magnetization profiles can be easily tuned to program the centimeter-scale structures' deformation.

B. Multimodal Crawling Locomotion of Magnetic Soft Robots

The static theoretical model can be further used to predict the quasi-static motions, enabling the programmable multimodal crawling locomotion of the HMSM beams. Crawling

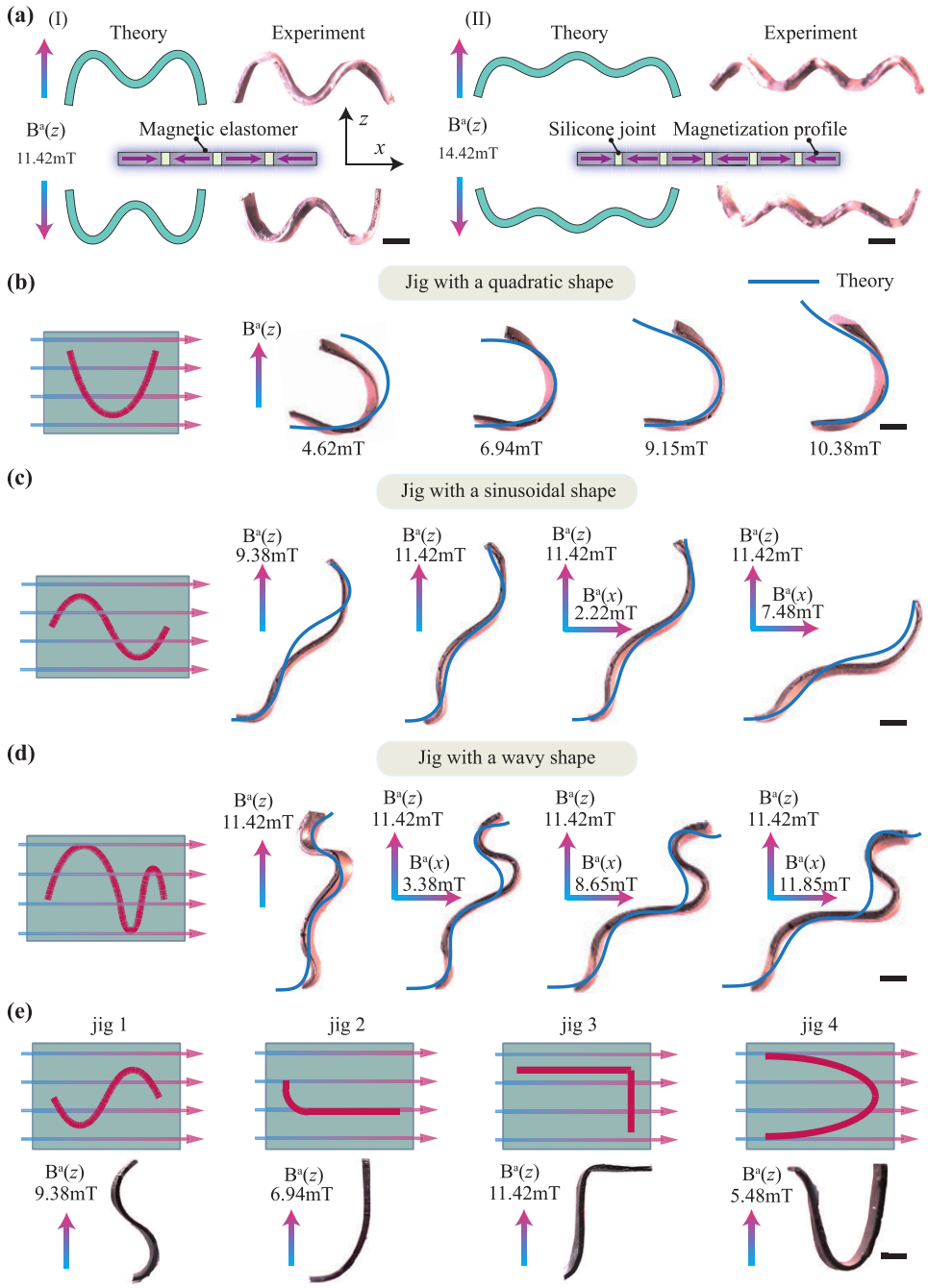

Fig. 4. Programming HMSM beams with varying magnetization profiles. (a) HMSM beams with four or six magnetic unit cells assembled are designed. The magnetic unit cells are connected using silicone joints with alternating magnetization directions. (b-d) Theoretical and experimental deformed HMSM beams with varying magnetization profiles produced by jigs with different shapes: (b) a quadratic, (c) a sinusoidal, and (d) a wavy shape. The designed jigs for magnetization are shown schematically. The applied magnetic fields are given. (e) Four HMSM beams deform into "SJTU" logo shape. All scale bars are 5 mm.

is an efficient and fast way to sweep across solid terrains [47], [48], [49], [50]. The key to producing crawling motion is to break the self-symmetry. Self-symmetry generally leads to a contraction or extension with respect to its center, while breaking the symmetry can generate a net gain that converts the stored elastic energy into translational motion [50]. Many demonstrations of crawling movements have been shown before [8], [23], [50]. However, designs of crawling motions based on theoretical models are rare. Here, we present three different methods to break self-symmetry: varying particle volume fraction, using asymmetric $\mathbf{B}_0^r$ and using asymmetric magnetic field.

Fig. 5(a) uses varying particle volume fractions to break self-symmetry. Two different volume fractions (left half $\varphi = 10\%$, right half $\varphi = 20\%$) are used for the HMSM beam. It is programmed using multiple symmetric polylines. Therefore, the difference in the particle volume fraction will generate different torque under an external magnetic field, which causes asymmetry in the deformed shapes. The deformed shapes of the HMSM beam in a period are shown and compared with the

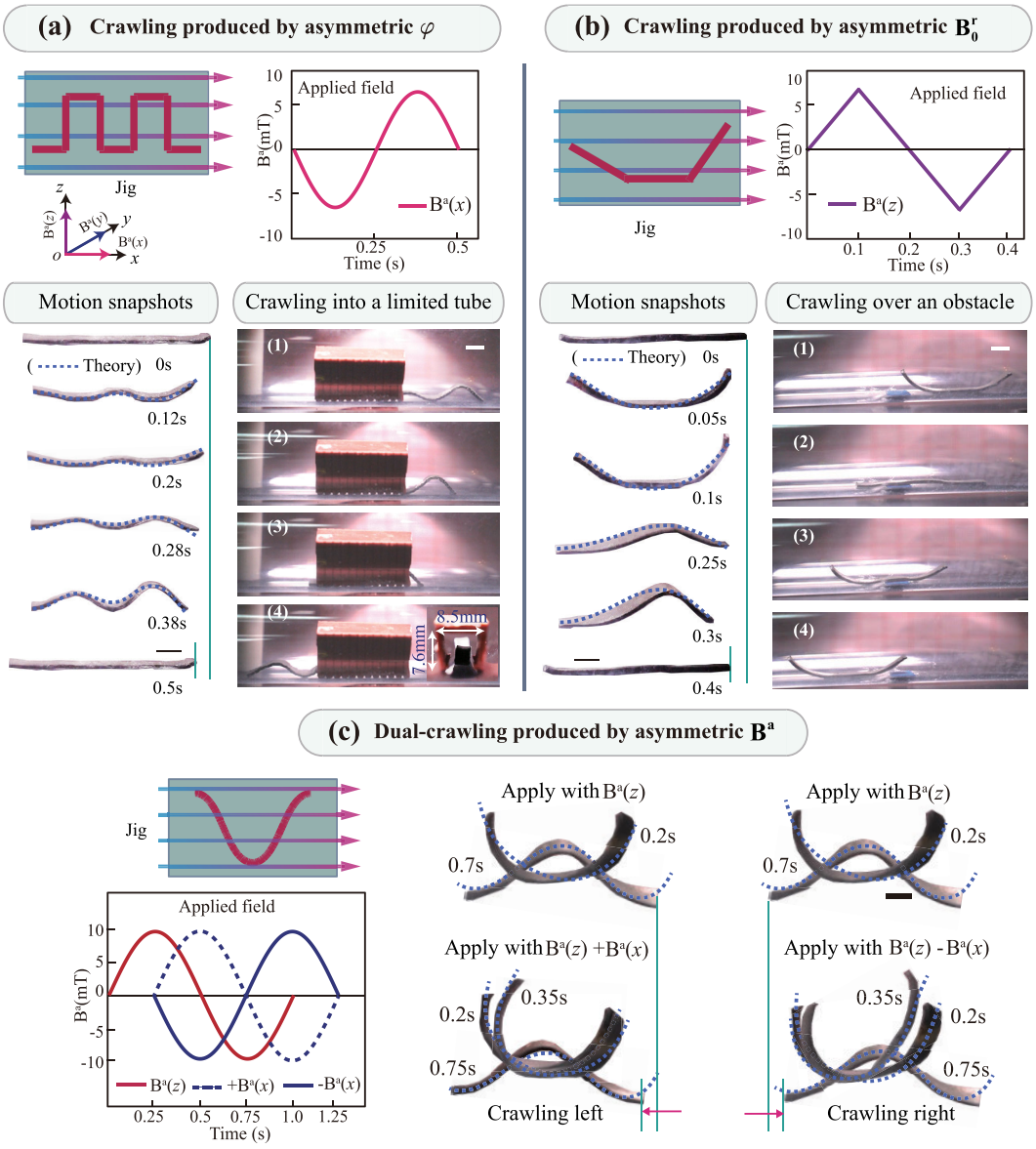

Fig. 5. Design of multimodal crawling of HMSM soft robots by breaking the self-symmetry. (a) Crawling motion produced by asymmetric particle volume fraction. The soft robot crawls into a hollow cube ($l \times w \times h$=42×8.5 × 7.6 mm). (b) Crawling motion produced by asymmetric magnetization profile. The soft robot climbs over a obstacle (7 × 5.5×2 mm). (c) Dual-direction crawling produced by asymmetric magnetic actuating. After magnetization using a cosine jig, the soft robot shows a dual-direction crawling mode under a switching magnetic field. Analytical results are overlapped for comparison. All scale bars are 5 mm.

theoretical predictions. Due to the large φ, the displacement on the right side of the beam is larger. Under the oscillating magnetic field, the beam forms an asymmetric wave-like motion. The wave-like movement, coupled with the change of contact conditions with the substrate, drives the soft robots to move in the left direction. The experimental snapshots and theoretically predicted shapes at various times are shown. The theoretical model predicts well the deformed shapes. The HMSM beams successfully crawl into a cube with a speed of 0.85 mm/s, which indicates the HMSM beams' potential to work in limited workspaces (Movie 6).

Asymmetric $\mathbf{B}_0^{\mathbf{r}}$ breaks self-symmetry in Fig. 5(b), generated using a multiple polylines jig with three different slopes. The asymmetric also breaks the self-symmetry and forms a crawling motion. Due to the larger slope, the right end flips at a larger speed. It can be observed that the wave crest exists on the right side. Similar to Fig. 5(a), the asymmetric $\mathbf{B}_0^{\mathbf{r}}$ wave drives the soft robots to the left direction under a synergic effect of the magnetic field and the contact interaction with the ground. Theoretical predictions agree well with the experimental shapes. The experiment in Fig. 5(b) also demonstrates that the beam can climb over an obstacle (7 × 5.5×2 mm) due to the large deflection on the front side.

Another way to generate asymmetry is to use an asymmetric magnetic field, as shown in Fig. 5(c). Besides an oscillating $\mathbf{B}^{\mathbf{a}}(z)$, a $\mathbf{B}^{\mathbf{a}}(x)$ is applied with a shifted phase. It can be observed that the soft robot moves in the left direction when the $\mathbf{B}^{\mathbf{a}}(x)$ represented by the dashed blue curve is applied. On the contrary, the soft robot moves in the right direction when an inverse $\mathbf{B}^{\mathbf{a}}(x)$ is used (solid blue curve). The

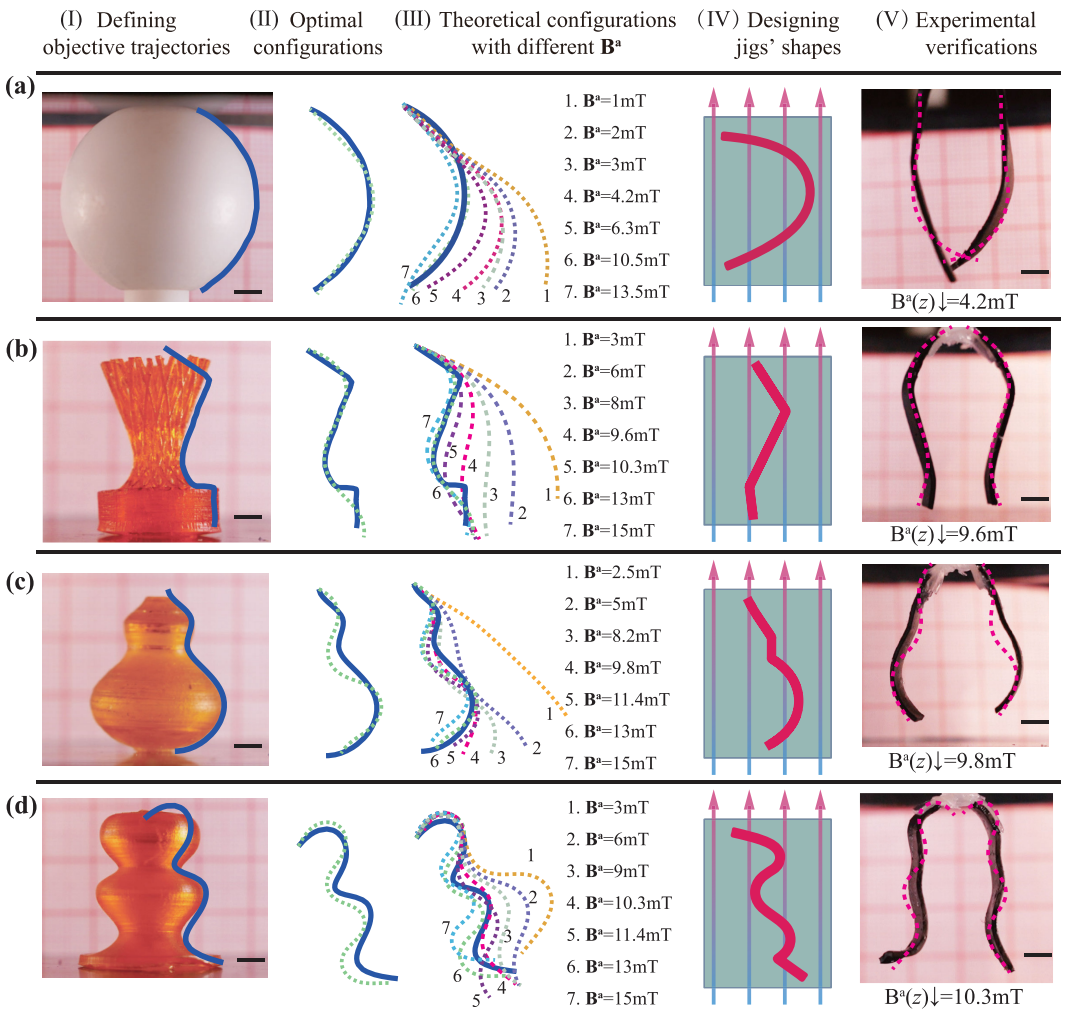

Fig. 6. Inverse design of HMSM soft grippers. (I) Objective trajectories (blue solid) are extracted from the surface contours of four objects: (a) a ball, (b) a vase, (c) a calabash and (d) a dumbbell. (II) The comparisons between the optimal configurations (green dot) and the objective trajectories. (III) Theoretical prediction deformed shapes under various applied fields. The magnitudes of the applied fields are shown. (IV) Jigs are designed based on optimized parameters. (V) Comparisons between the experimental and predicted deformed shapes under given applied fields. All the scale bars are 5 mm.

superposition of the two magnetic fields produces a more prominent deflection peak, which benefits the conversion of the stored strain energy to translational motion. The theoretical modeling can reasonably predict the experimental shapes. A soft robot with a dual-direction crawling motion at a speed of 3 mm/s is shown in Fig. 5(c) and Movie 6. The capability to crawl in dual-direction benefits motion control and retrieval after use.

C. Inverse Design of Magnetic Soft Grippers

Magnetic soft grippers have the advantages of rapid, untethered and reversible actuation [18], [51], [52], [53]. With an increased demand for robust and efficient grasping, magnetic soft grippers should have the capability of interacting with objects depending on their morphologies. However, the existing magnetic grippers generally exhibit simple bending deformations with constant curvatures. It works well for objects with regular surfaces (i.e., eggs, bulbs, cubes), but it remains challenging to interact with objects with complex morphologies [18], [51], [54], [55], [56]. The proposed analytical model can be used to optimize the deformed shapes inversely, enabling the matching with the objects' surface contours and reducing the stress concentration. The centimeter-scale soft robots can form various deformations and motions similar to millimeter-scale soft robots, while possessing a larger workspace.

As shown in Fig. 6(I), the soft magnetic grippers are optimized to grasp four different objects. Fig. 6(II) compares the optimized configurations and objective curves. The deformed shapes of the HMSM grippers under various applied fields are theoretically predicted (Fig. 6(III)). To validate the inverse design method, the optimal HMSM grippers are fabricated. The corresponding magnetization jigs are designed by (1) (Fig. 6(IV)). Fig. 6(V) presents the optimized grippers' experimental and theoretical deformed configurations. Good agreements are observed. The optimized beams are further used to grasp the objects (Movie 7). Note that the optimal applied field may be too large to be used in the experiments due to the limitation of the magnetic field generator, which is one of the main reasons for the discrepancies. The weights of the four objects are 24, 5, 6 and 5.5 times heavier than the grippers, respectively. The constrained ranges and the

optimized results as given in Table S4. Three magnetic soft grippers are fabricated without optimization for comparison (Fig.S7 and S8 and Movie 8). Compared with miniature magnetic grippers, the optimized centimeter-scale gripper show an improved grasping capacity, which can fulfill complex tasks in unstructured environments. Additionally, we have compared the gripping ability of the optimized results with the soft grippers that fixed directly to the contour of objects and then magnetized in Fig. S11. Although the unoptimized grippers exhibited a similar deformation tendency to the optimized grippers, they cannot lift the objects when subjected to the same magnetic actuation. Therefore, the optimized algorithm improves the grasping ability of complex structures.

V. Conclusion and Discussion

This work presents a centimeter-scale hard-magnetic soft robot with varying magnetization profiles that can match specific shapes under an external magnetic field. To inversely design the deformed configurations, a theoretical framework is proposed that establishes the relationship between the geometric (beam's length), material (magnetization profile, magnetic particle volume fraction) and loading parameters (external magnetic field) with the deformed shapes. The theoretical framework is based on the minimum potential energy method and takes into account the varying magnetization profile and gravity effect. The elastic energy, Helmholtz's energy, and gravitational potential energy are expressed as functions of the axial and bending strain. By setting the variation of the potential energy as zero, the two parameters can be solved, and the deformed shapes can be reconstructed. Experiments are conducted to validate the theoretical model. The validated analytical model is then used to design the deformed shape via an inverse optimization method.

In this study, we consider the effect of geometric nonlinearity while disregarding material nonlinearity. Although the HMSM beam exhibits significant bending deformation, the corresponding strain is relatively small. By conducting a FE simulation, we calculate the maximal principal strain of a cantilevered HMSM beam ($40 \times 5 \times 1$ mm) under a vertically applied magnetic field (12 mT), as illustrated in Fig. S6. Despite the substantial overall deformation, the strain remains below 5%. Hence, the assumption of linear elasticity is justified, leading to accurate results that align with experimental observations.

Linear elasticity has been widely employed in modeling magnetically-responsive soft materials. For instance, Chen et al. [33] utilized the small strain assumption to determine the deformation of functionally graded hard magnetic soft beams. Sano et al. [29] developed a Kirchhoff-like theory to describe the geometrically nonlinear deformation of HMSM rods in three dimensions, based on an elastic energy function. Yan et al. [57] employed Euler's elastic equation to solve the bending energy of HMSM beams subjected to uniform and gradient magnetic fields.

To precisely capture the behaviors of HMSM structures, it is crucial to consider nonlinear elasticity. Dorfmann and Ogden [58] established a comprehensive finite deformation framework of magneto-sensitive elastomers by incorporating the Maxwell equation, mechanical balance law, and thermodynamic equation. Zhao et al. [3] developed a finite deformation model for three-dimensional HMSM using Neo-Hookean material. Ye et al. [40] proposed a lattice model to simulate the nonlinear deformation of HMSM. Furthermore, more complex scenarios, such as viscoelastic effects [59], instability behaviors [60], and dynamic responses [61], have also been investigated. The nonlinearities present in magnetically-responsive soft materials are of significant importance and will be explored in our future research.

Once the HMSM is magnetized with a specific magnetization profile, the magnetization in the HMSM is fixed. Therefore, its deformation under a particular magnetic field is fixed, which poses a challenge in navigating diverse obstacles. Progress has been made to improve the adaptability of magnetic soft robots recently, including controlling the applied magnetic field sophisticatedly, using reconfigurable materials and structure, and developing re-magnetized method. For instance, Hu et al. [8] presented a miniature magnetic soft robot capable of jumping over obstacles by controlling the magnetic field. Using origami structure, Ze et al. [62] demonstrated an origami magnetic robot that integrated multimodal locomotion, liquid medicine delivery, and cargo transportation. Sun et al. [14] developed a slime robot with reconfigurable significant deformation by virtue of non-Newtonian fluid-based magnetic materials. Alapan et al. [51] developed reprogrammable magnetic soft machines using a high-throughput magnetic programming strategy based on heating magnetic soft materials above the Curie temperature to reorient their magnetic domains. These studies serve as valuable references for the future endeavors in improving the adaptability of magnetic soft robots.

Multimodal grasping and crawling motion are demonstrated to show the capability of the proposed theoretical framework. Directional crawling is realized by breaking the self-symmetry in three ways: asymmetric particle volume fraction, asymmetric magnetization profile and asymmetric magnetic field. Quasi-static deformed shapes are predicted by the theoretical model, which enables the design of soft locomotion robots with multiple functions, such as passing through narrow spaces or overcoming obstacles. Soft grippers that can exhibit prescribed grasping postures are designed using the inverse optimization method. The centimeter-scale soft robots exhibit larger workspace and output forces than the millimeter-scale soft robots.

The major contributions can be summarized as follows. First, we develop a theoretical framework for hard-magnetic soft robots based on the minimum potential energy that takes into account the varying magnetization profiles and gravity effect.

Secondly, the theoretical model directly relates the input parameters, such as the material, geometric and loading parameters, to the final deformation. Thus, it can be used to program the deformed shapes by adjusting the input parameters. Results show that the deformed configurations can be programmed by tuning the applied magnetic field, the particle volume fraction, the magnetization profile, etc.

Algorithm 1 Algorithm for Predicting the Deformation of HMSM Beam

Input: The given magnetic field $\mathbf{B^a}$ normalized by P, the magnetization profile $\mathbf{B_0^r}$, the length to deform s.
Output: The coordinates of deformed HMSM beam (X, Z).

1. Initialization;
2. Discretization of domain;
3. Define function: ODE of θ; ▷: Eq. (15)
4. Define function: BC of θ; ▷: Eq. (16)
5. Define the initial solution θ_0 by setting the guess values at the initial mesh point equal to the boundary values;
6. Set relative and absolute tolerances "tol" of the solver;
7. **While** $p < P$ do
8. $[\theta^n] =$ **bvp4c**(ODE of θ, BC of θ, θ_0);
9. Evaluate solution using deval function;
10. **Update** θ_0;
11. Increment: $p = p + P$, and $n = n + 1$;
12. Solve the axial strain $[\varepsilon^n]$ using $\mathbf{B^a}$,$\mathbf{B_0^r}$; ▷: Eq. (14)
13. Calculate the integral of the displacement (u, v) during one revolution; ▷: Eq. (6), Eq. (7)
14. **Return** $[X, Z]$.

Algorithm 2 Algorithm for Inverse Design

Input: The objective trajectory m(s).
Output: The desired $\mathbf{B^a}$ and $\mathbf{B_0^r}(s)$.

1. Initialization;
2. Discretization of m(s) with N points;
3. Design an initial magnetization profile $\mathbf{B_0^r}(s_0)$ using the basic elementary functions;
4. Set the lower and upper bounds on the design variables in s;
5. Set the constrain in **fmincon** function;
6. Set design variables starting point in **fmincon** function;
7. Calculate the initial shape m(s_0); ▷: Eq. (14), Eq. (15)
8. Discretization of m(s_0) with N points;
9. Calculate the distances between m(s) and m(s_0) using **distance2curve** function ▷: Eq. (18);
10. Call for **fmincon** function;
11. **Repeat**;
12. Update $\mathbf{B_0^r}(s_0)$;
13. Update m(s_0);
14. **Until** $\min\left(\sum_{i=1}^{N}(\Delta d_i)^2\right)$ is satisfied;
15. **Return** the desired $\mathbf{B^a}$ and $\mathbf{B_0^r}$.

Thirdly, the theoretical model is used to design centimeter-scale soft locomotion robots by breaking self-symmetry. The soft robots can crawl with programmable shapes by breaking the symmetry in magnetization profile, magnetic field and particle volume fraction.

Finally, an optimization method is proposed by virtue of the analytical model, enabling the inverse design of soft grippers that follow particular deformed shapes. Soft grippers matching the complex surface of objects are designed. The proposed design method has immense potential to design centimeter-scale soft robots with untethered magnetic actuation and broaden their applications.

APPENDIX
ALGORITHMS

See Algorithms 1 and 2.

SUPPLEMENTARY MATERIALS

Details on experiments, theoretical results and videos are shown in Supplementary Materials.

REFERENCES

[1] Y. Kim, H. Yuk, R. Zhao, S. A. Chester, and X. Zhao, "Printing ferromagnetic domains for untethered fast-transforming soft materials," *Nature*, vol. 558, no. 7709, pp. 274–279, Jun. 2018.

[2] G. Z. Lum et al., "Shape-programmable magnetic soft matter," *Proc. Nat. Acad. Sci. USA*, vol. 113, no. 41, pp. E6007–E6015, 2016.

[3] R. Zhao, Y. Kim, S. A. Chester, P. Sharma, and X. Zhao, "Mechanics of hard-magnetic soft materials," *J. Mech. Phys. Solids*, vol. 124, pp. 244–263, Mar. 2019.

[4] L. S. Novelino, Q. Ze, S. Wu, G. H. Paulino, and R. Zhao, "Untethered control of functional origami microrobots with distributed actuation," *Proc. Nat. Acad. Sci. USA*, vol. 117, no. 39, pp. 24096–24101, Sep. 2020.

[5] L. Yang, Y. Zhang, Q. Wang, K.-F. Chan, and L. Zhang, "Automated control of magnetic spore-based microrobot using fluorescence imaging for targeted delivery with cellular resolution," *IEEE Trans. Autom. Sci. Eng.*, vol. 17, no. 1, pp. 490–501, Jan. 2020.

[6] M. Zafar et al., "Performance analysis of magnetic nanoparticles during targeted drug delivery: Application of OHAM," *Comput. Model. Eng. Sci.*, vol. 130, no. 2, pp. 723–749, 2022.

[7] X. Du et al., "Reconfiguration, camouflage, and color-shifting for bioinspired adaptive hydrogel-based millirobots," *Adv. Funct. Mater.*, vol. 30, no. 10, 2020, Art. no. 1909202.

[8] W. Hu, G. Z. Lum, M. Mastrangeli, and M. Sitti, "Small-scale soft-bodied robot with multimodal locomotion," *Nature*, vol. 554, no. 7690, pp. 81–85, Feb. 2018.

[9] Y. Kim, G. A. Parada, S. Liu, and X. Zhao, "Ferromagnetic soft continuum robots," *Sci. Robot.*, vol. 4, no. 33, Aug. 2019, Art. no. eaax7329.

[10] Z. Ren et al., "Soft-bodied adaptive multimodal locomotion strategies in fluid-filled confined spaces," *Sci. Adv.*, vol. 7, no. 27, Jul. 2021, Art. no. eabh2022.

[11] L. Song et al., "Motion control of capsule robot based on adaptive magnetic levitation using electromagnetic coil," *IEEE Trans. Autom. Sci. Eng.*, early access, Sep. 23, 2022, doi: 10.1109/TASE.2022.3201966.

[12] C. Fu, J. Lu, W. Ge, C. Tan, and B. Li, "A review of electromagnetic energy regenerative suspension system & key technologies," *Comput. Model. Eng. Sci.*, vol. 135, no. 3, pp. 1779–1824, 2023.

[13] X. Fan, X. Dong, A. C. Karacakol, H. Xie, and M. Sitti, "Reconfigurable multifunctional ferrofluid droplet robots," *Proc. Nat. Acad. Sci. USA*, vol. 117, no. 45, pp. 27916–27926, Nov. 2020.

[14] M. Sun et al., "Reconfigurable magnetic slime robot: Deformation, adaptability, and multifunction," *Adv. Funct. Mater.*, vol. 32, no. 26, Jun. 2022, Art. no. 2112508.

[15] D. Lin, N. Li, N. Jiao, Z. Wang, and L. Liu, "Kinematic analysis of multi-section opposite magnetic catheter robots with solution multiplicity," *IEEE Trans. Autom. Sci. Eng.*, early access, Dec. 19, 2022, doi: 10.1109/TASE.2022.3229416.

[16] Z. Wang, S. Guo, J. Guo, Q. Fu, L. Zheng, and T. Tamiya, "Selective motion control of a novel magnetic-driven minirobot with targeted drug sustained-release function," *IEEE/ASME Trans. Mechatronics*, vol. 27, no. 1, pp. 336–347, Feb. 2022.

[17] E. Diller and M. Sitti, "Three-dimensional programmable assembly by untethered magnetic robotic micro-grippers," *Adv. Funct. Mater.*, vol. 24, no. 28, pp. 4397–4404, Jul. 2014.

[18] Q. Ze et al., "Magnetic shape memory polymers with integrated multifunctional shape manipulation," *Adv. Mater.*, vol. 32, no. 4, Jan. 2020, Art. no. 1906657.

[19] S. Wu, C. M. Hamel, Q. Ze, F. Yang, H. J. Qi, and R. Zhao, "Evolutionary algorithm-guided voxel-encoding printing of functional hard-magnetic soft active materials," *Adv. Intell. Syst.*, vol. 2, no. 8, 2020, Art. no. 2000060.

[20] E. Diller, J. Zhuang, G. Zhan Lum, M. R. Edwards, and M. Sitti, "Continuously distributed magnetization profile for millimeter-scale elastomeric undulatory swimming," *Appl. Phys. Lett.*, vol. 104, no. 17, Apr. 2014, Art. no. 174101.

[21] T. Xu, J. Yu, C.-I. Vong, B. Wang, X. Wu, and L. Zhang, "Dynamic morphology and swimming properties of rotating miniature swimmers with soft tails," *IEEE/ASME Trans. Mechatronics*, vol. 24, no. 3, pp. 924–934, Jun. 2019.

[22] Y. Cheng et al., "A fast autonomous healing magnetic elastomer for instantly recoverable, modularly programmable, and thermorecyclable soft robots," *Adv. Funct. Mater.*, vol. 31, no. 32, Aug. 2021, Art. no. 2101825.

[23] Y. Ju et al., "Reconfigurable magnetic soft robots with multimodal locomotion," *Nano Energy*, vol. 87, Sep. 2021, Art. no. 106169.

[24] C. Li et al., "Fast and programmable locomotion of hydrogel-metal hybrids under light and magnetic fields," *Sci. Robot.*, vol. 5, no. 49, Dec. 2020, Art. no. eabb9822.

[25] N. Xia et al., "Decoupling and reprogramming the wiggling motion of midge larvae using a soft robotic platform," *Adv. Mater.*, vol. 34, no. 17, Apr. 2022, Art. no. 2109126.

[26] Y. Xu, K. Li, Z. Zhao, and M. Q.-H. Meng, "A novel system for closed-loop simultaneous magnetic actuation and localization of WCE based on external sensors and rotating actuation," *IEEE Trans. Autom. Sci. Eng.*, vol. 18, no. 4, pp. 1640–1652, Oct. 2021.

[27] D. Lin, N. Jiao, Z. Wang, and L. Liu, "A magnetic continuum robot with multi-mode control using opposite-magnetized magnets," *IEEE Robot. Autom. Lett.*, vol. 6, no. 2, pp. 2485–2492, Apr. 2021.

[28] L. Wang, Y. Kim, C. F. Guo, and X. Zhao, "Hard-magnetic elastica," *J. Mech. Phys. Solids*, vol. 142, Sep. 2020, Art. no. 104045.

[29] T. G. Sano, M. Pezzulla, and P. M. Reis, "A kirchhoff-like theory for hard magnetic rods under geometrically nonlinear deformation in three dimensions," *J. Mech. Phys. Solids*, vol. 160, Mar. 2022, Art. no. 104739.

[30] Q. Zhang and S. Rudykh, "Magneto-deformation and transverse elastic waves in hard-magnetic soft laminates," *Mech. Mater.*, vol. 169, Jun. 2022, Art. no. 104325.

[31] W. Chen and L. Wang, "Theoretical modeling and exact solution for extreme bending deformation of hard-magnetic soft beams," *J. Appl. Mech.*, vol. 87, no. 4, Apr. 2020, Art. no. 041002.

[32] W. Chen, L. Wang, Z. Yan, and B. Luo, "Three-dimensional large-deformation model of hard-magnetic soft beams," *Composite Struct.*, vol. 266, Jun. 2021, Art. no. 113822.

[33] W. Chen, Z. Yan, and L. Wang, "On mechanics of functionally graded hard-magnetic soft beams," *Int. J. Eng. Sci.*, vol. 157, Dec. 2020, Art. no. 103391.

[34] W. Chen, Z. Yan, and L. Wang, "Complex transformations of hard-magnetic soft beams by designing residual magnetic flux density," *Soft Matter*, vol. 16, no. 27, pp. 6379–6388, 2020.

[35] D. Garcia-Gonzalez and M. Hossain, "Microstructural modelling of hard-magnetic soft materials: Dipole–dipole interactions versus Zeeman effect," *Extreme Mech. Lett.*, vol. 48, Oct. 2021, Art. no. 101382.

[36] D. Garcia-Gonzalez and M. Hossain, "A microstructural-based approach to model magneto-viscoelastic materials at finite strains," *Int. J. Solids Struct.*, vols. 208–209, pp. 119–132, Jan. 2021.

[37] R. Ortigosa, J. Martínez-Frutos, C. Mora-Corral, P. Pedregal, and F. Periago, "Optimal control and design of magnetic field-responsive smart polymer composites," *Appl. Math. Model.*, vol. 103, pp. 141–161, Mar. 2022.

[38] L. Wang, D. Zheng, P. Harker, A. B. Patel, C. F. Guo, and X. Zhao, "Evolutionary design of magnetic soft continuum robots," *Proc. Nat. Acad. Sci. USA*, vol. 118, no. 21, May 2021, Art. no. e2021922118.

[39] Z. Zhao and X. S. Zhang, "Topology optimization of hard-magnetic soft materials," *J. Mech. Phys. Solids*, vol. 158, Jan. 2022, Art. no. 104628.

[40] H. Ye, Y. Li, and T. Zhang, "Magttice: A lattice model for hard-magnetic soft materials," *Soft Matter*, vol. 17, no. 13, pp. 3560–3568, 2021.

[41] D. Hua, X. Liu, S. Sun, M. A. Sotelo, Z. Li, and W. Li, "A magnetorheological fluid-filled soft crawling robot with magnetic actuation," *IEEE/ASME Trans. Mechatronics*, vol. 25, no. 6, pp. 2700–2710, Dec. 2020.

[42] X. Hu, Z. Ge, X. Wang, N. Jiao, S. Tung, and L. Liu, "Multifunctional thermo-magnetically actuated hybrid soft millirobot based on 4D printing," *Composites B, Eng.*, vol. 228, Jan. 2022, Art. no. 109451.

[43] S. Ahmed and F. R. Jones, "A review of particulate reinforcement theories for polymer composites," *J. Mater. Sci.*, vol. 25, no. 12, pp. 4933–4942, Dec. 1990.

[44] C. Semler, G. X. Li, and M. P. Païdoussis, "The non-linear equations of motion of pipes conveying fluid," *J. Sound Vibrat.*, vol. 169, no. 5, pp. 577–599, Feb. 1994.

[45] T. F. Coleman and Y. Li, "An interior trust region approach for nonlinear minimization subject to bounds," *SIAM J. Optim.*, vol. 6, no. 2, pp. 418–445, May 1996.

[46] J. Vaicekauskaite, P. Mazurek, S. Vudayagiri, and A. L. Skov, "Mapping the mechanical and electrical properties of commercial silicone elastomer formulations for stretchable transducers," *J. Mater. Chem. C*, vol. 8, no. 4, pp. 1273–1279, 2020.

[47] E. B. Joyee and Y. Pan, "A fully three-dimensional printed inchworm-inspired soft robot with magnetic actuation," *Soft Robot.*, vol. 6, no. 3, pp. 333–345, Jun. 2019.

[48] H. Niu et al., "MagWorm: A biomimetic magnet embedded worm-like soft robot," *Soft Robot.*, vol. 8, no. 5, pp. 507–518, Oct. 2021.

[49] Q. Ze et al., "Soft robotic origami crawler," *Sci. Adv.*, vol. 8, no. 13, Apr. 2022, Art. no. eabm7834.

[50] S. Wu et al., "Symmetry-breaking actuation mechanism for soft robotics and active metamaterials," *ACS Appl. Mater. Interfaces*, vol. 11, no. 44, pp. 41649–41658, Nov. 2019.

[51] Y. Alapan, A. C. Karacakol, S. N. Guzelhan, I. Isik, and M. Sitti, "Reprogrammable shape morphing of magnetic soft machines," *Sci. Adv.*, vol. 6, no. 38, Sep. 2020, Art. no. eabc6414.

[52] G. Mao et al., "Soft electromagnetic actuators," *Sci. Adv.*, vol. 6, no. 26, Jun. 2020, Art. no. eabc0251.

[53] C. Pacchierotti et al., "Steering and control of miniaturized untethered soft magnetic grippers with haptic assistance," *IEEE Trans. Autom. Sci. Eng.*, vol. 15, no. 1, pp. 290–306, Jan. 2018.

[54] S. R. Goudu, I. C. Yasa, X. Hu, H. Ceylan, W. Hu, and M. Sitti, "Biodegradable untethered magnetic hydrogel milli-grippers," *Adv. Funct. Mater.*, vol. 30, no. 50, Dec. 2020, Art. no. 2004975.

[55] Z. Ji, C. Yan, B. Yu, X. Wang, and F. Zhou, "Multimaterials 3D printing for free assembly manufacturing of magnetic driving soft actuator," *Adv. Mater. Interfaces*, vol. 4, no. 22, Nov. 2017, Art. no. 1700629.

[56] B. Sun et al., "Magnetic arthropod millirobots fabricated by 3D-printed hydrogels," *Adv. Intell. Syst.*, vol. 4, no. 1, Jan. 2022, Art. no. 2100139.

[57] D. Yan, A. Abbasi, and P. M. Reis, "A comprehensive framework for hard-magnetic beams: Reduced-order theory, 3D simulations, and experiments," *Int. J. Solids Struct.*, vol. 257, Dec. 2022, Art. no. 111319.

[58] A. Dorfmann and R. W. Ogden, "Magnetoelastic modelling of elastomers," *Eur. J. Mech. A/Solids*, vol. 22, no. 4, pp. 497–507, Jul. 2003.

[59] D. Garcia-Gonzalez, "Magneto-visco-hyperelasticity for hard-magnetic soft materials: Theory and numerical applications," *Smart Mater. Struct.*, vol. 28, no. 8, Aug. 2019, Art. no. 085020.

[60] P. Pathak, N. Arora, and S. Rudykh, "Magnetoelastic instabilities in soft laminates with ferromagnetic hyperelastic phases," *Int. J. Mech. Sci.*, vol. 213, Jan. 2022, Art. no. 106862.

[61] W. Huang, M. Liu, and K. J. Hsia, "A discrete model for the geometrically nonlinear mechanics of hard-magnetic slender structures," *Extreme Mech. Lett.*, vol. 59, Mar. 2023, Art. no. 101977.

[62] Q. Ze et al., "Spinning-enabled wireless amphibious origami millirobot," *Nature Commun.*, vol. 13, no. 1, p. 3118, Jun. 2022.

Jinqiang Wang received the B.Eng. degree from the College of Mechanical and Vehicle Engineering, Hunan University, China, in 2016, and the M.Eng. degree from the College of Mechanical and Electrical Engineering, Nanjing University of Aeronautics and Astronautics, China, in 2019. He is currently pursuing the Ph.D. degree in mechanical engineering with the Shanghai Jiao Tong University, China.

His research interests include 4D printing and soft robotics, especially the modeling and design of magnetic actuation robotics.

Dong Wang received the B.E. degree in mechanical engineering from Zhejiang University, China, in 2010, and the Ph.D. degree in mechanical engineering from Nanyang Technology University, Singapore, in 2015.

Since October 2018, he has been with Shanghai Jiao Tong University, where he is currently appointed as an Associate Professor with the School of Mechanical Engineering. He is the author or coauthor of over 40 publications. His research interests include soft robotics, 3D and 4D printing, and solid mechanics.

Le Dong received the B.E. degree from the Huazhong University of Science and Technology in 2020. He is currently pursuing the Ph.D. degree with the Institute of Robotics, Shanghai Jiao Tong University.

His research interests include theoretical modeling and the design of multi-material metamaterials.

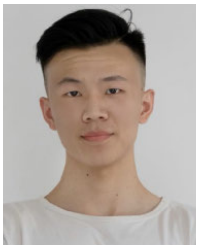

Mengjie Zhang received the B.E. degree from the College of Mechanical Engineering, Chongqing University, China, in 2020. He is currently pursuing the Ph.D. degree with the School of Mechanical Engineering, Shanghai Jiao Tong University, China.

His research interests include 3D and 4D printing.

Guoying Gu (Senior Member, IEEE) received the B.E. degree (Hons.) in electronic science and technology and the Ph.D. degree (Hons.) in mechatronic engineering from Shanghai Jiao Tong University, Shanghai, China, in 2006 and 2012, respectively.

Since October 2012, he has been with Shanghai Jiao Tong University, where he is currently appointed as a Professor with the School of Mechanical Engineering. He was a Humboldt Fellow of the University of Oldenburg, Germany. He was a Visiting Scholar with the Massachusetts Institute of Technology, National University of Singapore, and Concordia University. His research interests include soft robotics, bioinspired and wearable robots, smart materials sensing, actuation, and motion control. He is the author or coauthor of over 100 publications, which have appeared in *Nature Biomedical Engineering*, *Science Robotics*, *Science Advances*, *Advanced Materials*, *National Science Review*, IEEE/ASME TRANSACTIONS, *Advanced Functional Materials*, and *Soft Robotics*, as book chapters and in conference proceedings.

Dr. Gu received the National Science Fund for Distinguished Young Scholars. He also serves as an Associate Editor for IEEE TRANSACTIONS ON ROBOTICS and IEEE ROBOTICS AND AUTOMATION LETTERS. He has also served for several journals as an editorial board member, a topic editor, or a guest editor, and several international conferences/symposiums as the chair, the co-chair, and an associate editor or a program committee member.